

NUMERICAL SOLUTION OF WATER ENTRY PROBLEM
OF 2-D WEDGES

MIN ZHANG



**Numerical Solution of Water Entry Problem of
2-D wedges**

by

© Min Zhang
St. John's, Newfoundland, Canada

A thesis submitted to the
School of Graduate Studies
in partial fulfillment of the
requirements for the degree of
Master of Engineering

Faculty of Engineering and Applied Science
Memorial University of Newfoundland

June 2011

Abstract

The numerical solution of nonlinear water entry problem for two-dimensional (2-D) wedges is presented in this thesis. The Boundary Element Method (BEM) was used for solving the Laplace equation, and the Mixed Eulerian Lagrangian scheme was employed to track the nonlinear free surface. The free surface profile and the velocity potential are represented by Cubic-Splines. The forward fourth-order Runge-Kutta method was used for time marching. A cut-off treatment was applied to the thin jet to avoid computational instability.

Verification studies were carried out for a wavemaker with impulsive motions. Pressure distributions, free surface elevations and hydrodynamic forces were calculated and compared with analytical solutions and other numerical results. The developed numerical method was then employed to solve the symmetric water entry of 2-D wedges with various deadrise angles. Pressure distributions and free surface elevations were compared with experimental results and solutions by other numerical methods, such as the similarity method, BEM, and the constrained interpolation profile (CIP) method.

Acknowledgements

I wish to express my sincere thanks to my supervisor Dr. Wei Qiu, who suggested the research topic, for his encouragement, guidance and constructive discussions during the development of this thesis. Also, I appreciate the guidance from my co-supervisor Dr. Heather Peng.

I deeply appreciate the financial support of the Natural Sciences and Engineering Research Council (NSERC) of Canada, the Mathematics of Information Technology and Complex Systems (MITACS) and the Graduate Fellowship from Memorial University. Without their support, this work could not have been possibly completed.

Many thanks are extended to my colleagues at the Advanced Marine Hydrodynamics Lab (AMHL), for the useful discussions and suggestions throughout my work. I also would like to acknowledge advices from Dr. Hinchey.

Finally, I would like to give my special thanks to my family. I am profoundly grateful for their love, support and understanding.

Contents

Chapter1	Introduction	1
1.1	Literature Review	2
1.2	Summary of the Present Work	5
1.3	Thesis Contents	6
Chapter2	Mathematical Formulation	7
2.1	Governing Equation	7
2.2	Boundary Conditions.....	7
2.3	Initial Conditions.....	9
2.4	Hydrodynamic pressure.....	10
2.5	Boundary Element Method (BEM).....	12
2.6	Time-Marching Scheme	16
2.7	Regridding by Parametric Cubic Splines	19
2.8	Cut- off treatment of the jet flow	21
2.9	Summary of the Computational Procedure	23
Chapter3	Numerical Results and Discussions	25
3.1	Impulsive Wavemaker Motion	25
3.1.1	Grid generation in the chosen domain.....	26
3.1.2	Free surface elevations, pressure distributions and hydrodynamic forces	29
3.2	Symmetric water entry of 2-D Wedges.....	35
3.2.1	Grid generation in the chosen domain.....	35
3.2.2	Free surface elevations and pressure distributions	37
3.3	Symmetric water entry of 2-D wedges with various deadrise angles	56

Chapter4	Conclusions	70
----------	-------------------	----

List of figures

Figure 1-1 Slamming Examples.....	1
Figure 2-1 Coordinate system and definitions (Sun, 2007).....	8
Figure 2-2 Elements, mid-points on the boundary.....	15
Figure 2-3 Procedure of regriding free surface with parametric Cubic Splines	21
Figure 2-4 Cut-off treatment of the jet flow (Sun, 2007)	22
Figure 2-5 Flow chart of computational procedure	24
Figure 3-1 Snapshot of impulsive wavemaker (Lin, 1983).....	26
Figure 3-2 Grids on the wave tank boundaries.....	27
Figure 3-3 Velocity potential on the wavemaker at $t=0^+$	28
Figure 3-4 Velocity potential on the wavemaker for different Rt_s	29
Figure 3-5 Free surface elevation at $t=0.025s$	29
Figure 3-6 Free surface elevation at $t=0.050s$	30
Figure 3-7 Free surface elevation at $t=0.105s$	30
Figure 3-8 Free surface elevation at $t=0.145s$	31
Figure 3-9 Free surface elevation at $t=0.195s$	31
Figure 3-10 Pressure distribution on the wavemaker at $t=0.05s$	32
Figure 3-11 Pressure distribution on the wavemaker at $t=0.10s$	33
Figure 3-12 Pressure distribution on the wavemaker at $t=0.25s$	33
Figure 3-13 Pressure distribution on the wavemaker at $t=0.40s$	34
Figure 3-14 Horizontal force acting on the wavemaker	35
Figure 3-15 Grids on the fluid domain boundaries.....	36
Figure 3-16 Grids near the intersection point	36
Figure 3-17 Pressure distributions for different grid sizes on wedge	37
Figure 3-18 Free surface elevations for different lengths of equal-sized grids	38

Figure 3-19 Free surface elevation of the wedge with deadrise angle of 60° at $t=0.006s$	39
Figure 3-20 Free surface elevation of the wedge with deadrise angle of 60° at $t=0.012s$	39
Figure 3-21 Free surface elevation of the wedge with deadrise angle of 60° at $t=0.018s$	40
Figure 3-22 Free surface elevation of the wedge with deadrise angle of 60° at $t=0.024s$	40
Figure 3-23 Free surface elevation of the wedge with deadrise angle of 60° at $t=0.03s$	41
Figure 3-24 Snapshot of water entry of wedge with deadrise angle of 60° (Lin, 1983)	41
Figure 3-25 Pressure distribution on wedge with deadrise angle of 60° at $t=0.006s$	42
Figure 3-26 Pressure distribution on wedge with deadrise angle of 60° at $t=0.012s$	43
Figure 3-27 Pressure distribution on wedge with deadrise angle of 60° at $t=0.018s$	43
Figure 3-28 Pressure distribution on wedge with deadrise angle of 60° at $t=0.024s$	44
Figure 3-29 Pressure distribution on wedge with deadrise angle of 60° at $t=0.03s$	44
Figure 3-30 Free surface elevation of the wedge with deadrise angle of 45° at $t=0.006s$	45
Figure 3-31 Free surface elevation of the wedge with deadrise angle of 45° at $t=0.012s$	46
Figure 3-32 Free surface elevation of the wedge with deadrise angle of 45° at $t=0.018s$	46
Figure 3-33 Free surface elevation of the wedge with deadrise angle of 45° at $t=0.024s$	47
Figure 3-34 Free surface elevation of the wedge with deadrise angle of 45° at $t=0.03s$	47
Figure 3-35 Snapshot of water entry of wedge with deadrise angle of 45° (Lin, 1983)	48
Figure 3-36 Pressure distribution on wedge with deadrise angle of 45° at $t=0.006s$	48
Figure 3-37 Pressure distribution on wedge with deadrise angle of 45° at $t=0.012s$	49
Figure 3-38 Pressure distribution on wedge with deadrise angle of 45° at $t=0.018s$	49
Figure 3-39 Pressure distribution on wedge with deadrise angle of 45° at $t=0.024s$	50
Figure 3-40 Pressure distribution on wedge with deadrise angle of 45° at $t=0.03s$	50
Figure 3-41 Free surface elevation of the wedge with deadrise angle of 30° at $t=0.024s$	51
Figure 3-42 Free surface elevation of the wedge with deadrise angle of 30° at $t=0.03s$	52
Figure 3-43 Free surface elevation of the wedge with deadrise angle of 30° at $t=0.039s$	52
Figure 3-44 Free surface elevation of the wedge with deadrise angle of 30° at $t=0.048s$	53

Figure 3-45 Free surface elevation of the wedge with deadrise angle of 30° at $t=0.057s$	53
Figure 3-46 Pressure distribution on the wedge with deadrise angle of 30° at $t=0.024s$	54
Figure 3-47 Pressure distribution on the wedge with deadrise angle of 30° at $t=0.03s$	54
Figure 3-48 Pressure distribution on the wedge with deadrise angle of 30° at $t=0.039s$	55
Figure 3-49 Pressure distribution on the wedge with deadrise angle of 30° at $t=0.048s$	55
Figure 3-50 Pressure distribution on the wedge with deadrise angle of 30° at $t=0.057s$	56
Figure 3-51 Free surface elevation of the wedge with deadrise angle of 81° at $t=0.045s$	57
Figure 3-52 Pressure distribution on the wedge with deadrise angle of 81° at $t=0.045s$	57
Figure 3-53 Free surface elevation of the wedge with deadrise angle of 75° at $t=0.045s$	58
Figure 3-54 Pressure distribution on the wedge with deadrise angle of 75° at $t=0.045s$	58
Figure 3-55 Free surface elevation of the wedge with deadrise angle of 70° at $t=0.057s$	59
Figure 3-56 Pressure distribution on the wedge with deadrise angle of 70° at $t=0.057s$	59
Figure 3-57 Free surface elevation of the wedge with deadrise angle of 65° at $t=0.057s$	60
Figure 3-58 Pressure distribution on the wedge with deadrise angle of 65° at $t=0.057s$	60
Figure 3-59 Free surface elevation of the wedge with deadrise angle of 55° at $t=0.024s$	61
Figure 3-60 Pressure distribution on the wedge with deadrise angle of 55° at $t=0.024s$	61
Figure 3-61 Free surface elevation of the wedge with deadrise angle of 50° at $t=0.024s$	62
Figure 3-62 Pressure distribution on the wedge with deadrise angle of 50° at $t=0.024s$	62
Figure 3-63 Free surface elevation of the wedge with deadrise angle of 40° at $t=0.036s$	63
Figure 3-64 Pressure distribution on the wedge with deadrise angle of 40° at $t=0.036s$	63
Figure 3-65 Free surface elevation of the wedge with deadrise angle of 35° at $t=0.036s$	64
Figure 3-66 Pressure distribution on the wedge with deadrise angle of 35° at $t=0.036s$	64
Figure 3-67 Free surface elevation of the wedge with deadrise angle of 25° at $t=0.036s$	65
Figure 3-68 Pressure distribution on the wedge with deadrise angle of 25° at $t=0.036s$	65
Figure 3-69 Free surface elevation of the wedge with deadrise angle of 20° at $t=0.036s$	66
Figure 3-70 Pressure distribution on the wedge with deadrise angle of 20° at $t=0.036s$	66

Figure 3-71 Free surface elevation of the wedge with deadrise angle of 15° at $t=0.0495s$	67
Figure 3-72 Pressure distribution on the wedge with deadrise angle of 15° at $t=0.0495s$	67
Figure 3-73 Free surface elevation of the wedge with deadrise angle of 10° at $t=0.0558s$	68
Figure 3-74 Pressure distribution on the wedge with deadrise angle of 10° at $t=0.0558s$	68

Nomenclature

F	hydrodynamic force
$G_{i,j}$, $H_{i,j}$	influence coefficient matrices
Δl	length of elements
n	unit normal vector
p_0	atmospheric pressure
p	hydrodynamic pressure
S	boundary of the fluid domain
S_B	bottom surface
S_C	symmetric surface
S_F	free surface
S_R	right-end surface

S_w	wavemaker surface
Δt	time step
U	velocity of wavemaker
V	velocity of wedges
$X(x,y)$	Cartesian coordinates
y_0	submergence of the wedge apex
α	deadrise angle
ρ	water density
η	free surface elevation
Ω	fluid domain
ϕ	velocity potential

Chapter1 Introduction

Slamming is of concern in many marine applications. The resultant forces are sometimes sufficient to deform the structure of a ship or an offshore structure. In addition, slamming is a source of fatigue for offshore structures, which may result in structural damages over time. Examples of ship slamming phenomena are given in Fig.1-1.



Figure 1-1 Slamming Examples

Slamming loads, as defined by Faltinsen (1990), are impulsive loads with high pressure peaks occurring during impact between a body and water. This is characterized by large hydrodynamic loads in a short period of time, such as wetdeck slamming, green water and sloshing in ship tanks. Slamming is usually caused by large relative vertical motions between wave and body, which will lead to prominent nonlinear effects. The typical forms of the nonlinearity are shown as thin jets and sprays, non-viscous flow separation, and wave breaking etc. In addition, compressibility of air and water, air

bubbles and hydroelasticity may be involved. The combination of the above factors makes the slamming problems very complicated (Faltinsen, 2004).

Given the complex nature of slamming, some simplified slamming models have been investigated by many researchers before the complete simulations of slamming are applied to ships. One of the most extensively studied slamming phenomena is the water entry of 2-D wedges into an initially calm free surface. In this thesis, a numerical method has been investigated to solve the water entry of 2-D wedges into calm water.

1.1 Literature Review

The studies of 2-D wedges entering water with an initially calm free surface are motivated by the slamming of ship bows or sterns in heavy seas. These difficult problems are usually solved by simplifying the model as a rigid body entering initially calm water with a free surface. Due to the rapid entry of the wedges into water, viscous effects are negligible. The compressibility and air-cushion effects only matter in a short period of time after impact between the body and the free surface.

The pioneering contributions in this field were made by Von Karman (1929). Von Karman used a flat plate approximation in the simulation, which underestimated loads for small deadrise angles. Armand and Cointe (1986), Cointe (1991) and Howison et al. (1991) extended Wagner's theory to analyze the water entry problem using matched asymptotic expansions. The limitation of above studies was that it required the impacting body to be nearly parallel to the calm free surface, i.e., with small deadrise angles.

Another way of solving the water entry problem was first put forward by Dobrovol'skaya (1969), which provided a similarity method for the symmetric water entry of a wedge of infinite extent with constant velocity. Fully-nonlinear free surface

conditions and the exact body boundary conditions were satisfied in his method. However, the solutions were not given in an explicit form and limited by the assumptions of symmetric body shape, constant water entry speed and gravity was not accounted for.

In addition to the above two approaches, numerical methods have also been extensively developed to solve the nonlinear water entry problem and have become the mainstream of research in this area. The advantage of numerical methods is that there are theoretically no restrictions for the body shape and the water entry speed while gravity can also be included. The Boundary Element Method (BEM) based on potential theory and the CFD (Computational Fluid Dynamics) methods based on Navier-Stokes equations are the commonly used to simulate the nonlinear water entry problems.

For the CFD methods, many researchers have contributed to the simulations of slamming. For example, Kleefsman et al. (2005) used the volume of fluid (VOF) method to investigate a dambreak problem and water entry problems. Kim et al. (2007) used the smoothed particle hydrodynamics (SPH) method to simulate the water entry of asymmetric bodies. Yang and Qiu (2007) applied the constrained interpolation profile (CIP) method to solve the slamming problem of 2-D wedges entering water.

CFD methods are more time-consuming and more demanding in computer capacity compared to BEM. Many efforts have been made to solve the problem of 2-D wedges entering water with an initially calm free surface based on the BEM. The first successful numerical simulation of 2-D steep water surface motions and overturning waves was made by Longuet-Higgins and Cokelet (1976), in which Laplace equation was solved by BEM based on Green's function and the free surface was updated by the Mixed Eulerian-Lagrangian method (MEL). Vinje and Brevig (1981) modified their method based on Cauchy's complex integral theorem. Greenhow and Lin (1987) later used this method to solve the water entry problem. However, their results were only satisfactory for deadrise angles larger than 60 degrees, because of the instability of

computations caused by the thin jet along the wedge side for small deadrise angles. In addition, this method can only be applied to 2-D problems due to the nature of the complex integral theorem. However, the exact description of the thin jet is not necessary because the pressure in the jet is nearly atmospheric and it has little influence on other parts of the fluid. Zhao and Faltinsen (1993, 1996) developed a BEM with a cut-off treatment of the jet flow to avoid the numerical instability. A new segment was introduced at the jet root and the upper part of jet region was removed. They used the finite difference method to calculate the time derivative of the velocity potential, and then computed the hydrodynamic pressures. However, this method in general can not give good accuracy of the pressure distributions. In addition, the method for representing the free surface at each time step was not convenient to use.

Based on Zhao and Faltinsen (1993)'s work, Lin and Ho (1994) introduced linear elements, instead of the constant element, to evaluate the free surface elevations and potential derivatives. The benefit of using linear elements was that the flow field near the intersection point can be described numerically with physical meaning. However, the pressures were still computed using the finite difference method. Later, the free surface was better represented using cubic splines or non-uniform rational B-splines (NURBS) to increase the accuracy. Battistin and Iafrati (2003) introduced cubic splines to describe and discretize the free surface when evaluating hydrodynamic loads during water entry of 2-D axisymmetric bodies. Chuang and Zhu (2006) used NURBS to represent the body surface and the free surface profile when solving the 2-D water entry problem.

To improve the accuracy of the pressure, two methods are widely used to give a better prediction of pressure distributions in the recent studies. One is the complex velocity potential method. Greenhow and Lin (1987) used this method to evaluate slamming pressure for 2-D wedges entering water. Sun (2007) further developed Zhao (1993, 1996)'s method to compute pressure distributions. Wu et al. (2010) also used the complex velocity potential to solve the water entry problem in the stretched

coordinate system for a symmetrical wedge, an asymmetrical wedge and twin wedges. The other method to compute pressure distributions was developed by Tanizawa (1995), in which the time derivative of velocity potential was directly obtained from solving a boundary integral equation, then the pressure can be computed using Bernoulli's equation. Qian and Wang (2005) used this method to calculate pressures on ships and floating structures. Kihara (2004, 2008) applied the same method to compute pressure distributions for slamming problems. The latter method was adopted in this thesis, due to its less requirement for computing resources than the complex velocity potential method.

1.2 Summary of the Present Work

In this work, the numerical solution for 2-D nonlinear water entry problem was developed based on Zhao's method (1993). Other computational techniques were adopted in this work to improve both the accuracy and stability of computations in this thesis. The initial disturbance is simulated by Wagner's approximation (Sun, 2007). The forth-order Runge-Kutta scheme was used for the time integration and a five-point smoothing scheme was applied to eliminate numerical instability. The parametric cubic-splines were used to represent and discretize the free surface and velocity potential for each time instant. A scheme based on the work of Kihara (2004, 2008) has been developed for computing pressure distributions. The constant elements were used in the computation. The cut-off method was employed to deal with the intersection between the free surface and the body surface. In this work, the velocity was assumed constant and gravity was neglected.

The numerical method was first verified by applying it to the problem of impulsive wavemaker. Validation studies were then carried out to the symmetric water entry of 2-D wedges with various deadrise angles. Pressures, free surface elevations and hydrodynamic forces were computed and compared with experimental results,

analytical solutions, and solutions by other numerical methods.

1.3 Thesis Contents

This thesis is arranged as follows. Chapter 2 describes the mathematical formulation with regards to the numerical method. Firstly, the governing equation, boundary conditions and the related initial conditions are presented. Secondly, the Boundary Element Method (BEM) obtained from the Laplace equation and equations for hydrodynamic pressures are briefly described. Thirdly, the numerical implementation of the BEM in the time domain is revealed and the procedure for time marching is explained. Finally, the cut-off treatment of the thin jet flow and the Cubic Splines used for regriding of free surface profiles and velocity potentials are introduced. In Chapter 3, an impulsive wavemaker case is first computed to verify the developed method. The method is then employed to symmetric water entry of 2-D wedges with various deadrise angles. The free surface elevations, pressure distributions and hydrodynamic forces are subsequently obtained. Numerical results are compared with experimental results, analytical solutions and solutions by other numerical methods. Conclusions and recommendations are presented in Chapter 4.

Chapter2 Mathematical Formulation

2.1 Governing Equation

A Cartesian coordinate system $o-xy$, fixed in space is chosen with the origin at the undisturbed water level, with ox representing the horizontal direction and oy the vertical direction, positive upward, as shown in Fig. 2-1. It is assumed that the fluid is inviscid and incompressible and flow is irrotational. It is also assumed that there are no air cushions and no non-viscous flow separation. In addition, the fluid acceleration associated with initial impact is generally much larger than the gravitational acceleration, and the time duration that is investigated in this problem is much smaller compared to typical wave periods. Therefore, the effect of gravity is neglected. A velocity potential $\phi(x, y, t)$ satisfies the Laplace equation in the fluid domain Ω .

$$\frac{\partial^2 \phi}{\partial x^2} + \frac{\partial^2 \phi}{\partial y^2} = 0 \quad (2.1)$$

The water entry problem can be formulated as an initial boundary-value problem (BVP) for the velocity potential ϕ and solved with either Neumann or Dirichlet type of boundary conditions.

2.2 Boundary Conditions

For the problem of 2-D wedges entering water with an initially calm surface, only half of the fluid domain ($x > 0$) is studied due to the symmetrical property of the problem about the y -axis, as shown in Fig. 2-1.

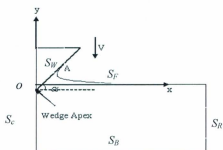


Figure 2-1 Coordinate system and definitions (Sun, 2007)

Fully nonlinear boundary conditions are imposed on the free surface S_f . The dynamic boundary condition on the free surface in the Lagrangian form is

$$\frac{D\phi}{Dt} = \frac{1}{2} |\nabla\phi|^2 - g\eta - p_0 \quad (2.2)$$

satisfied on the exact free-surface, where $\eta = \eta(X, t)$ is the instantaneous free-surface elevation and p_0 is the pressure on the free-surface assumed to be zero. If the effect of gravity is neglected compared to the large fluid acceleration, it can be rewritten as

$$\frac{D\phi}{Dt} = \frac{1}{2} \left[\left(\frac{\partial\phi}{\partial x} \right)^2 + \left(\frac{\partial\phi}{\partial y} \right)^2 \right] \quad (2.3)$$

The kinematic boundary conditions on the free surface in the Lagrangian form are expressed as

$$\frac{Dx}{Dt} = \frac{\partial\phi}{\partial x} \quad (2.4)$$

$$\frac{Dy}{Dt} = \frac{\partial \phi}{\partial y} \quad (2.5)$$

Along the wedge, a kinematic boundary condition is imposed as

$$\frac{\partial \phi}{\partial n} = \mathbf{V} \cdot \mathbf{n} \quad (2.6)$$

where \mathbf{V} is the velocity vector of wedge and \mathbf{n} is the unit normal vector on the wedge pointing out of the fluid.

The no-flux boundary condition imposed on the bottom S_b , on the far field S_∞ and on the symmetric boundary S_c is

$$\frac{\partial \phi}{\partial n} = 0 \quad (2.7)$$

2.3 Initial Conditions

Initially, the velocity potential is zero on the undisturbed free surface.

$$\phi(X, 0) = 0 \quad (2.8)$$

For the water entry problem, the initial disturbance on free surface profile caused by the impact between wedge and water has to be taken into account. Based on the work of Sun (2007), the following Wagner's approximation method to simulate the initial free surface elevation is employed.

$$\eta(x,0) = \frac{xy_0}{c} \arcsin\left(\frac{c}{x}\right) - y_0 \quad (2.9)$$

$$c = \frac{\pi y_0}{2 \tan \alpha} \quad (2.10)$$

where y_0 is the submergence of wedge apex relative to the undisturbed free surface, and α is the deadrise angle (see Fig. 2-1).

2.4 Hydrodynamic pressure

The hydrodynamic pressure p can be computed according to the Bernoulli's equation.

$$p - p_a = -\rho(gz + \frac{\partial \phi}{\partial t} + \frac{1}{2} |\nabla \phi|^2) \quad (2.11)$$

where p_a is the atmospheric pressure and ρ is the water density. Since the influence of gravity can be neglected, the equation can be rewritten as

$$p - p_a = -\rho\left(\frac{\partial \phi}{\partial t} + \frac{1}{2} |\nabla \phi|^2\right) \quad (2.12)$$

It can be easily seen that the time derivative of the velocity potential $\partial \phi / \partial t$ must be computed in order to obtain pressure. Although it can be computed by applying the finite difference method to the velocity potential as in the work of Zhao (1993) and Lin (1984), the computational accuracy of the pressure is generally not sufficient. For more accurate prediction, the time derivative of the velocity potential $\partial \phi / \partial t$ can be obtained by solving the Laplace equation for $\partial \phi / \partial t$ with the following boundary conditions according to the work of Kihara (2004).

$$\nabla^2 \phi = 0 \quad \text{in } \Omega \quad (2.13)$$

$$\frac{\partial \phi_i}{\partial n} = \kappa |\nabla \phi|^2 + \frac{\partial \phi}{\partial n} \frac{\partial^2 \phi}{\partial s^2} - \frac{\partial \phi}{\partial s} \frac{\partial}{\partial s} \frac{\partial \phi}{\partial n} \quad \text{on } S_w \quad (2.14)$$

$$\phi_i = -\frac{1}{2} |\nabla \phi|^2 - gy \quad \text{on } S_f \quad (2.15)$$

$$\frac{\partial \phi_i}{\partial n} = 0 \quad \text{on } S_B, S_C, S_R \quad (2.16)$$

where $\partial/\partial s$ is the tangential derivative along the body surface, and κ denotes the local curvature of the body contour. The general form of the normal derivative of ϕ_i on the body in motion in Eq. 2.14 was simplified for the translational motion with constant velocity by Tanizawa (1995).

The initial condition is necessary to complete the problems, which is given as

$$\phi_i = 0 \quad \text{at } t = 0 \quad (2.17)$$

The procedure of solving for ϕ_i is similar to that of solving for velocity potential ϕ . Since the influence matrices for ϕ_i are same as those for ϕ , no additional matrix setup or inversion is necessary when solving the boundary integral equation for ϕ_i . Therefore, this method for solving for ϕ_i will not intensify the computations.

Integrating the pressure along the body surface S_w will result in the force F

$$F = \int_{S_w} p n ds \quad (2.18)$$

where p is the pressure distribution, and n is the unit normal vector on the wedge surface.

2.5 Boundary Element Method (BEM)

The Boundary Element Method has been very successfully used in the solving 2-D and 3-D wave-body interactions. In such problems, the method offers the great advantage of describing the flow by its boundary values only. Therefore, the dimensions of problems are reduced by one. Moreover, in the analysis of wave-body interaction, the only information needed in the computation is the boundary geometry, velocity potential and its flux on the boundary. Applications of BEM to nonlinear wave-body interaction problems essentially consist of two coupled parts. The first is a solution of the Laplace equation at a given time. The second part is a forward stepping to the next time instant at which the Laplace equation is solved repeatedly.

In BEM, the Laplace equation is converted to a Boundary Integral Equation (BIE) by introducing Green's function $G(p, q) = -\frac{1}{2\pi} \ln r_{pq}$, where $r_{pq} = |p - q|$, p is the field point and q is the source point. The BIE obtained by applying Green's second identity to $\phi(x, y, t)$ and $G(p, q)$ is given as

$$\phi(p) + \int_S \phi(q) \frac{\partial G(p, q)}{\partial n(q)} dS_q = \int_S G(p, q) \frac{\partial \phi(q)}{\partial n(q)} dS_q \quad (2.19)$$

where S represents the boundaries of the fluid domain. When the field point p is on the boundary S , Eq. 2.19 can be rewritten as

$$\frac{1}{2} \phi(p) + \int_S \phi(q) \frac{\partial G(p, q)}{\partial n(q)} dS_q = \int_S G(p, q) \frac{\partial \phi(q)}{\partial n(q)} dS_q \quad (2.20)$$

In the numerical evaluation of Eq. 2.20, free surface S_f , body surface S_w , bottom surface S_b and far field boundary S_∞ are divided into a number of constant elements,

on which ϕ and $\partial\phi/\partial n$ are constant. Eq. 2.20 can be rewritten in the discretized form as

$$\frac{1}{2}\phi(p) + \sum_{j=1}^N \phi(q) \int_{s_j} \frac{\partial G(p,q)}{\partial n(q)} ds_q = \sum_{j=1}^N \frac{\partial\phi(q)}{\partial n(q)} \int_{s_j} G(p,q) dS_q \quad (2.21)$$

where N is the number of elements distributed on the boundaries.

Generally speaking, high resolution is needed to describe the free surface close to the intersections with high curvature. In the region close to the intersections, finer elements are used while elements with larger size are distributed on the boundaries far away from the intersections. However, it is not preferable that the ratio of the largest and the smallest elements is overly high, since the drop in computational accuracy may lead to numerical instability, especially in the region where the velocity gradient is high. According to Kihara (2004), the ratio of lengths of two adjacent elements should be no more than 3 in order to keep the computation stable. The effect of different ratios of lengths of adjacent elements will be presented in Chapter 3. In addition, in order to use the smoothing scheme, equal-size elements are used on part of the free surface near the intersections, while larger elements are distributed on the rest of the free surface. It should be noted that the control of spatial discretization during computation is vital to both the stability of the computation and accuracy of the results.

Introducing

$$\begin{aligned} \overline{H}_{i,j} &= -\frac{1}{2\pi} \int_{s_j} \frac{\partial}{\partial n_q} \ln(r_{pq}) ds_j \\ G_{i,j} &= -\frac{1}{2\pi} \int_{s_j} \ln(r_{pq}) ds_j \end{aligned} \quad (2.22)$$

Eq. 2.21 becomes

$$\frac{1}{2}\phi + \sum_{j=1}^n \overline{H}_{i,j} \phi_j = \sum_{j=1}^n G_{i,j} \left(\frac{\partial\phi}{\partial n} \right)_j \quad (2.23)$$

Eq. 2.23 can be rewritten as

$$\sum_{j=1}^n H_{i,j} \phi_j = \sum_{j=1}^n G_{i,j} \left(\frac{\partial \phi}{\partial n} \right)_j \quad (2.24)$$

where $H_{i,j}$ and $G_{i,j}$ are the influence coefficient matrices.

$$\begin{aligned} H_{i,j} &= \bar{H}_{i,j} & \text{for } i \neq j \\ &= \bar{H}_{i,j} + \frac{1}{2} & \text{for } i = j \end{aligned} \quad (2.25)$$

The logarithmic singularity can arise when $i=j$, i.e., p coincides with q . For $i=j$,

$$\bar{H}_{i,i} = -\frac{1}{2\pi} \int \frac{\partial}{\partial n} \ln(r_{pq}) ds = 0 \quad (2.26)$$

due to the orthogonality of r_{pq} and n (Kytke, 1995).

$$\begin{aligned} G_{ii} &= \frac{1}{2\pi} \int \ln\left(\frac{1}{r_{pq}}\right) ds = \frac{1}{2\pi} 2 \int_0^1 \ln\left(\frac{2}{\xi l_i}\right) \frac{l_i}{2} d\xi \\ &= \frac{l_i}{2\pi} \left[\xi \ln\left(\frac{2}{l_i}\right) - \xi \ln \xi + \xi \right]_0^1 \\ &= \frac{l_i}{2\pi} \left[1 + \ln\left(\frac{2}{l_i}\right) \right] \end{aligned} \quad (2.27)$$

where l_i is the length of the element i . For $r_{pq} = \xi l_i / 2$, $r = 0$ at $\xi = 0$ and $r = \pm l_i / 2$ at $\xi = \pm 1$.

For $i \neq j$, the integral for each element is evaluated by the 4-point Gaussian

quadrature.

$$\begin{aligned}
 H_{i,j} &= -\frac{1}{2\pi} \int_{s_j} \frac{\partial}{\partial n_q} \ln(r_{pq}) ds_j \\
 &= -\frac{1}{2\pi} J \sum_{i=1}^4 w_i [n_x(\bar{x}_q - x_p) + n_y(\bar{y}_q - y_p)] / r_{pq}^2
 \end{aligned} \tag{2.28}$$

$$\begin{aligned}
 G_{i,j} &= -\frac{1}{2\pi} \int_{s_j} \ln(r_{pq}) ds_j \\
 &= -\frac{1}{2\pi} J \sum_{i=1}^4 w_i \left\{ \frac{1}{2} \ln [(\bar{x}_q - x_p)^2 + (\bar{y}_q - y_p)^2] \right\}
 \end{aligned} \tag{2.29}$$

$$\begin{aligned}
 \bar{x}_q &= \sum_{i=1}^4 \frac{1}{2} [(1-c_i)x_{q1} + (1+c_i)x_{q2}] \\
 \bar{y}_q &= \sum_{i=1}^4 \frac{1}{2} [(1-c_i)y_{q1} + (1+c_i)y_{q2}] \\
 J &= \frac{1}{2} l_q
 \end{aligned} \tag{2.30}$$

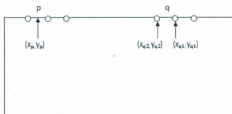


Figure 2-2 Elements, mid-points on the boundary

where x_p, y_p are the coordinates of midpoint on element p ; x_{q1}, y_{q1} are the coordinates of the first node of element q ; x_{q2}, y_{q2} are the coordinates of the second node of element q , as shown in Fig. 2-2; c_i are Gaussian quadrature coefficients and w_i are weights; J is the Jacobian of integration from global coordinate to local coordinate; and l_q is the length of the element q .

$$c_1 = -0.8611363d0$$

$$w_1 = 0.3478549d0$$

$$c_2 = -0.3399810d0$$

$$w_2 = 0.6521452d0$$

$$c_3 = 0.3399810d0$$

$$w_3 = 0.6521452d0$$

$$c_4 = 0.8611363d0$$

$$w_4 = 0.3478549d0$$

One can solve this matrix equation numerically using a scheme for linear system, such as the Gaussian elimination method. As for the pressure computation, the integral equation for time derivative of velocity potential can be solved in the same way.

At each time instant, by numerically solving the Eq. 2.20, the unknowns, both the velocity potential on each element, and the normal velocity on each element along the free surface can be obtained. The new free surface profile and velocity potential on the free surface for the next time instant can then be computed.

2.6 Time-Marching Scheme

When solving nonlinear free-surface problems, the exact free-surface boundary condition has to be satisfied on the exact free-surface position. The nonlinear wave problem was studied by Schwartz (1982) using the series expansion technique under the Eulerian description to approximate velocity potential and free surface elevation. However, the disadvantage of using the Eulerian description was that both the boundary conditions and the boundary position have to be approximated. To avoid this problem, an option is to employ Lagrangian description. In the Lagrangian description, the free-surface position is known, but the disadvantage of it is that the governing equation has to be approximated. A new numerical scheme called Mixed Eulerian-Lagrangian (MEL) method was developed by Longuet and Cokelet (1976), which can overcome the disadvantages of both the Eulerian and Lagrangian descriptions.

The MEL method was first used to simulate the time-history of steep surface waves. In the time marching, the surface was represented by marked Lagrangian fluid particles. This method requires that the integral equations are solved at each time step in the Eulerian frame, with fully nonlinear boundary conditions satisfied on the instant free surface and the body surface. The new position of the free surface for the next time instant can be found by integrating Eq. 2.3, Eq. 2.4 and Eq. 2.5. The x component of velocity $\partial\phi/\partial x$ and the y component of velocity $\partial\phi/\partial y$ can not be obtained directly from the BEM. However, from the velocity potential ϕ on the free surface, one can compute the tangential component of velocity $\partial\phi/\partial s$, combined with the normal component of velocity $\partial\phi/\partial n$ solved from the BEM, the x component of velocity $\partial\phi/\partial x$ and the y component of velocity $\partial\phi/\partial y$ can be expressed as

$$\begin{aligned}\frac{\partial\phi}{\partial x} &= \frac{\partial\phi}{\partial s}n_x + \frac{\partial\phi}{\partial n}n_y \\ \frac{\partial\phi}{\partial y} &= -\frac{\partial\phi}{\partial s}n_y + \frac{\partial\phi}{\partial n}n_x\end{aligned}\tag{2.31}$$

where n_x and n_y are the horizontal and vertical components of the unit normal vector $n(n_x, n_y)$ on the free surface, respectively. The tangential derivative of the velocity potential $\partial\phi/\partial s$ can be computed by using the finite difference method.

The time integration of Eq. 2.3, Eq. 2.4 and Eq. 2.5 is then performed by a forth-order Runge-Kutta (RK4) scheme, as shown below. The formulae for Runge-Kutta method are given by Burden and Faires (2005).

$$\begin{aligned}
d\omega / dt &= f(t, \omega) \\
k_1 &= \Delta t f(t, \omega) \\
k_2 &= \Delta t f\left(t, \omega + \frac{k_1}{2}\right) \\
k_3 &= \Delta t f\left(t, \omega + \frac{k_2}{2}\right) \\
k_4 &= \Delta t f(t_{n+1}, \omega + k_3) \\
\omega_{n+1} &= \omega_n + \frac{1}{6}(k_1 + 2k_2 + 2k_3 + k_4)
\end{aligned}
\tag{2.32}$$

where ω can be either x , y or ϕ . ω_i and ω_{i+1} are corresponding values at time step $n+1$ and n , and Δt is the time interval

During the time marching process, the sawtooth-type instability of the free surface occurs naturally when the integral equation is solved numerically. Longuet-Higgins and Cokelet (1976) adopted a five-point smoothing scheme to avoid the sawtooth phenomenon. However, the scheme is inapplicable to the first two and last two points on the surface. A smoothing scheme derived from the third-order least squares approximation over five points was introduced in this work (Sun, 2007).

It should be noted that the smoothing scheme is only applied to the near intersection region on the free surface where the free surface profile changes dramatically. This smoothing scheme can also be used to smooth out the x , y coordinates and the velocity potential ϕ . The first two equations of Eq. 2.33 are used for the first two points and the last two equations of Eq. 2.33 are employed to the last two points. The third one is used for the rest of the points.

$$\begin{aligned}
f_1 &= \frac{1}{70}(69y_1 + 4y_2 - 6y_3 + 4y_4 - y_5) \\
f_2 &= \frac{1}{35}(2y_1 + 27y_2 + 12y_3 - 8y_4 + 2y_5) \\
f_i &= \frac{1}{35}(-3y_{i-2} + 12y_{i-1} + 17y_i + 12y_{i+1} - 3y_{i+2}) \\
f_{N-1} &= \frac{1}{35}(2y_{N-4} - 8y_{N-3} + 12y_{N-2} + 27y_{N-1} + 2y_N) \\
f_N &= \frac{1}{70}(-y_{N-4} + 4y_{N-3} - 6y_{N-2} + 4y_{N-1} + 69y_N)
\end{aligned} \tag{2.33}$$

where y_i are the original values before smoothing and f_i are values after smoothing, and N is the total number of points on the free surface needed to be smoothed out.

The time step size Δt in the time marching procedure should be chosen with care, because a large Δt may lead to numerical instability while a small Δt will take unnecessary computational efforts. Based on the Courant–Friedrichs–Lewy condition (Roache, 1972 and Kihara, 2004), Δt was decided in consideration of the following condition:

$$\max\{|\nabla\phi_1|, |\nabla\phi_2|, \dots, |\nabla\phi_N|\} \times \Delta t \leq \frac{1}{3} \min\{\Delta l_1, \Delta l_2, \dots, \Delta l_N\} \tag{2.34}$$

where $\nabla\phi_i$ is the velocity of the midpoint on the element i , and Δl_i is the length of the element i .

2.7 Regridding by Parametric Cubic Splines

After updating the free surface by moving midpoints on each element at each time step, the new midpoints may become overly concentrated or scarce, especially in the region near the intersections, which is likely to cause computational instability. To avoid this phenomenon, regridding of the free surface at each instant is necessary. Parametric

cubic splines are chosen to interpolate the new node points and midpoints of each element, as well as the velocity potential on new midpoints. However, given the special property of the free surface that it can turn over on itself, parametric cubic splines using polygonal arc length is devised to approximate the free surface.

For parametric cubic splines, each spline segment is expressed in terms of an independent variable s as (Burden and Faires, 2005):

$$x_i(s) = a_i(s - s_0)^3 + b_i(s - s_0)^2 + c_i(s - s_0) + d_i \quad (2.35)$$

where s is the polygonal arc length from the first point of the cubic spline to the point of desire; s_0 is the polygonal arc length from the first point of the cubic spline to the starting point of any segment i ; x_i can be x coordinates, y coordinates or velocity potential to be computed. The coefficients a_i, b_i, c_i and d_i are calculated using known positions of the updated midpoints and continuity of the first and the second derivatives of x_i . In this work, the free surface was regrided by equal arc length and the distances were calculated from the first point on the splines to the evenly-spaced points. Based on the arc length, a corresponding cubic spline is chosen to compute the x, y coordinates and velocity potential of a desired point.

The whole process can be summarized into three steps, as shown in Fig. 2-3. Firstly, the midpoints A, B, C, D, E, F are updated to the new position A₁, B₁, C₁, D₁, E₁, F₁ from original free surface S. Secondly, parametric cubic splines are formulated to represent the new free surface S₁ using known positions of these updated midpoints and continuity of the first and the second derivatives. Thirdly, based on the given length of new elements, new nodes A₂, B₂, C₂, D₂, E₂ on the free surface S₁ can be calculated, as well as the midpoints of these elements and velocity potential on them. The new nodes form the new free surface S₂, which provides updated boundary conditions for next

time step.

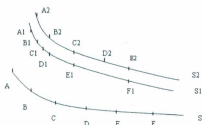


Figure 2-3 Procedure of regridding free surface with parametric Cubic Splines

2.8 Cut-off treatment of the jet flow

In the studies of nonlinear wave-body interactions, specially nonlinear free surface flow induced by impulsive motion, the loss of accuracy at the intersection points will occur. The so-called intersection point is where a thin jet and body surface meets on the free surface, such as point A shown in Fig. 2-1

According to the work of Sun (2007), a very thin jet will run up along the body surface when the body with impulsive motion impacts the water surface, especially when the contact angle between the body surface and the water surface is small. For the cases of small contact angles, computational errors can easily arise in the area of intersection point, in the form of some points going through body, which is physically impossible. This kind of errors causes the numerical code to collapse. The theoretical explanation of the problem is that the velocity becomes singular at the intersection points, that is, the velocity is infinite. Therefore, the thin jet flow must be properly treated.

Two aspects are needed to be considered in the treatment of the jet flow: one is the

computational accuracy, and the other is computational stability. The two are usually in conflict with one another. When finer elements are distributed near the intersections, more accurate results can be obtained, however, the computation easily gets unstable. On the other hand, when fewer elements are used close to the intersection points, the code becomes stable while the jet flow is hard to be simulated according to the work of Lin (1984). One of the commonly used methods to solve this problem is a cut-off treatment of the thin jet flow.

In the work of Zhao (1993), a new element normal to the wedge surface was employed to cut off the jet when the contact angle between the wedge surface and the free surface is smaller than a given value. Kihara (2004) also used the contact angle by introducing a new element to cut off the jet, however, the new element was not required to be normal to the wedge surface. Sun (2007) cut off the jet flow by introducing a threshold value of distance from the point next to the intersection point on the free surface to the wedge surface. A slightly different method from the one that Kihara (2004) used was derived in this work. Based on the fact that constant elements were employed in this work, it gave the flexibility to locate the position of intersection points. The cut-off treatment is illustrated in Fig. 2-4 for a wedge.

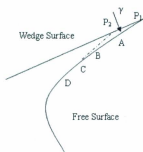


Figure 2-4 Cut-off treatment of the jet flow (Sun, 2007)

As shown in Fig. 2-4, A, B, C and D are updated midpoints on the free surface. Usually,

the intersection point is the intersection point P_1 of the wedge surface and the line AB. However, when the angle γ between the wedge surface and the line AB is smaller than a threshold value β , the line BC is then used to calculate the intersection point P_2 . If the contact angle between the wedge surface and the line BC is still smaller than β , the line CD is used instead until the contact angle is smaller than β .

The cut-off treatment allows for the simulation of the jet flow without compromising the stability of the numerical code. An important fact should be noted that the upper jet flow has little influence on the pressure distribution on the wedge surface or the rest of the free surface. The pressure is nearly equal to atmospheric pressure in the upper part of the jet. That is why the thin jet can be cut off in different ways without affecting results such as the profile of the rest of the free surface and pressure distribution on the wedge surface.

2.9 Summary of the Computational Procedure

The computational procedure can be summarized as the following flow chart. Starting with the initial boundary conditions, then use the BEM to obtain potential velocity ϕ on the wedge surface and its flux $\partial\phi/\partial n$ on the free surface. The tangential derivative of velocity potential $\partial\phi/\partial s$ on the free surface can be solved using the finite difference method based on the known potential velocity distribution on the free surface. Transforming $\partial\phi/\partial n$ and $\partial\phi/\partial s$ to $\partial\phi/\partial x$ and $\partial\phi/\partial y$, the free surface profile and velocity potential on the free surface can be updated for the next time instant. After updating the free surface by moving the midpoint on each element, the grids may be overly dense or scarce near the intersection point on the new free surface, therefore, parametric Cubic Splines are used to regrid the free surface and obtain velocity

potential on the new midpoints after the regridding. In order to make the computation stable, RK4 integral method and five-point smoothing scheme are employed in the time-stepping procedure. The new free surface profile and velocity potential on the free surface will then be used as the updated boundary conditions for the next time instant.

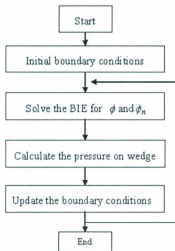


Figure 2-5 Flow chart of computational procedure

Chapter3 Numerical Results and Discussions

To verify the numerical method developed in this work, computations were first conducted for an impulsive wavemaker with prescribed motion. It is similar to, but less complicated than, the cases of symmetric 2-D wedges entering water. The present method was then applied to symmetric 2-D wedges with various deadrise angles. The time histories of pressure distributions, free surface elevations for both cases are presented and compared with experimental results, analytical solutions and numerical results obtained by the similarity method, BEM (Zhao,1993), and the CIP method (Yang, 2007).

3.1 Impulsive Wavemaker Motion

An impulsive wavemaker starts to move with a constant horizontal velocity U from a state of rest. At $t=0^+$, the velocity is a step function and the acceleration is infinite. Analytically, a logarithmic singularity is expected at the intersection point of the free surface and the wavemaker. This phenomenon is confirmed by the experiment performed by Lin (1983), shown in Fig. 3-1. It was noticed that the water rose up to a level that the wavemaker was almost parallel to it before a jet ejected from the intersection point. According to Lin (1983), the ejected jet quickly broke up under the effect of surface tension and possibly air currents generated by the wavemaker. Therefore, only the very short period of time after the impulsive wavemaker moved was investigated in this thesis.

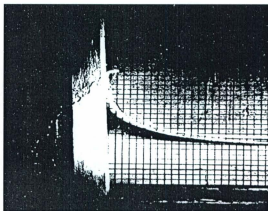


Figure 3-1 Snapshot of impulsive wavemaker (Lin, 1983)

3.1.1 Grid generation in the chosen domain

To simulate the motion of the impulsive wavemaker numerically, a fluid domain is chosen to be a long rectangular tank, as shown in Fig. 3-2. On the left-end boundary, a piston wavemaker performs prescribed impulsive motion and the right-end boundary is a rigid vertical wall. The length of the tank is 10m, which is long enough that influence of the reflection from the vertical wall can be avoided during the short period of computation. Water depth is 1m, and the horizontal velocity of the wavemaker is 1m/s. In the computation, the boundaries of the domain are discretized into a number of constant elements, on which ϕ and $\partial\phi/\partial n$ are set constant. The size of the elements varies along the boundaries, as shown in Fig. 3-2.

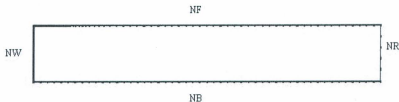


Figure 3-2 Grids on the wave tank boundaries

The number of elements is $NF=74$ on the free surface with the minimum size equal to 0.04m close to the intersection point of the free surface and wavemaker, $NW=25$ on the wavemaker, $NB=50$ on the bottom and $NL=5$ on the right-end wall at $t=0^+$. The size of time step needs to be sufficiently small. It was chosen as $dt=0.01s$ according to Eq. 2.37.

The velocity potential distributed on the wavemaker at $t=0^+$ is plotted in Fig. 3-3, and compared with the approximate analytical solution and numerical results by Lin (1984). The approximate analytical solution is given by Eq. 3.1 (Lin, 1984).

$$\begin{aligned} \phi_0 &= \sum_{n=0}^{\infty} \frac{2U}{dk_n^2} \sin k_n y \exp(-k_n x) \\ k_n &= \frac{(2n+1)\pi}{2d} \\ \eta &= -\frac{2U}{\pi} \log \left(\tanh \frac{\pi x}{4d} \right) \end{aligned} \quad (3.1)$$

The results by the present method agree well with other solutions. From Fig. 3-3, it can be seen that the slope of the velocity potential curve at $y=0$ is fairly steep. This suggests that the vertical velocity at the intersection is almost infinite at $t=0^+$, as predicted by the related theory.

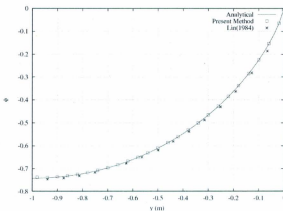


Figure 3-3 Velocity potential on the wavemaker at $t=0^+$

To investigate the influence of different ratios of lengths of adjacent elements on the velocity potential, a range of ratios of lengths are used to solve for the velocity potential on the wavemaker at $t=0^+$. Rl represents the ratio of lengths of adjacent elements. When the ratio Rl is equal to 5, the length of elements on the wavemaker is 0.04m while the length of elements on the bottom is 0.2m. When Rl is equal to 2.5, the length of elements on the wavemaker is 0.04m while the length of elements on the bottom is 0.1m. When Rl is equal to 1.25, the length of elements on the wavemaker is 0.04m while the length of elements on the bottom is 0.05m. The results for these ratios are plotted and shown in Fig. 3-4. It can be seen from this figure that the results near the intersection point of wavemaker and the bottom get closer to the analytical solution as the ratio approaches 1, which suggests that comparable sizes of adjacent elements can lead to more accurate results.

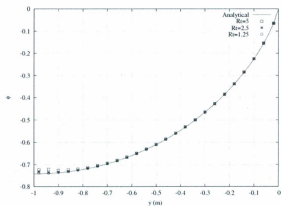


Figure 3-4 Velocity potential on the wavemaker for different Rt s

3.1.2 Free surface elevations, pressure distributions and hydrodynamic forces

For the subsequent time steps, comparisons of free surface elevations obtained by the present method, the analytical solution and Lin (1984) are presented at $t=0.025s$, $t=0.05s$, $t=0.105s$, $t=0.145s$ and $t=0.195s$ in Fig. 3-5 to Fig. 3-9, respectively.

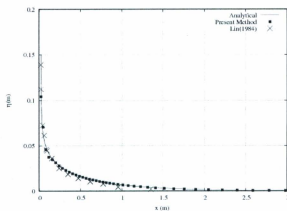


Figure 3-5 Free surface elevation at $t=0.025s$

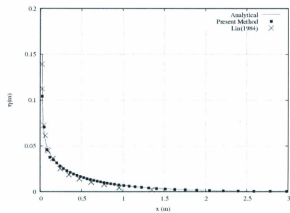


Figure 3-6 Free surface elevation at $t=0.050s$

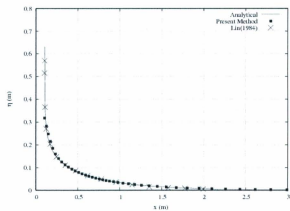


Figure 3-7 Free surface elevation at $t=0.105s$

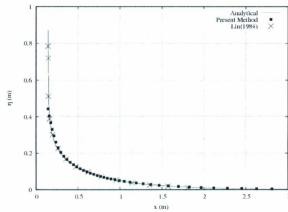


Figure 3-8 Free surface elevation at $t=0.145s$

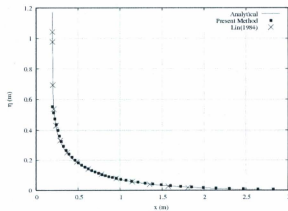


Figure 3-9 Free surface elevation at $t=0.195s$

It can be observed from these figures that the results of free surface elevations by the present method agree well with results from the analytical solution and Lin's method. The only remarkable difference is the position of the highest points in the plots, which is also the position of the intersection point of the free surface and the wavemaker. The

positions of intersection points given by present method are lower than Lin's results. This phenomenon becomes more obvious when the jet along the wavemaker gets higher. The reason is that a cut-off treatment of the jet flow is employed in present method based on the fact that the pressure in the thin jet along the wavemaker is almost equal to atmospheric pressure and does not contribute significantly to the total force acting on the wavemaker. In addition, the position of the highest point is closely related to the density of the grids in the intersection region. According to Lin (1984), the denser grids near the intersection will result in a very high intersection position but the rest of the free surface shape is not affected. On the other hand, the long and thin jet can easily cause computational instability. The advantages of current method over Lin's are fewer grids needed in the computation due to the cut-off technique used, hence less computational time, and better stability of the numerical codes.

Fig. 3-10 – Fig. 3-13 show comparisons of pressure distributions given by the present method and Lin (1984)'s method at $t=0.05s$, $t=0.10$, $t=0.25$, $t=0.40$, respectively.

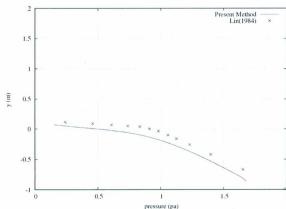


Figure 3-10 Pressure distribution on the wavemaker at $t=0.05s$

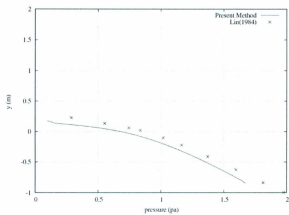


Figure 3-11 Pressure distribution on the wavemaker at $t=0.10s$

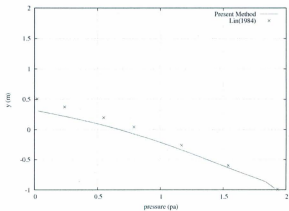


Figure 3-12 Pressure distribution on the wavemaker at $t=0.25s$

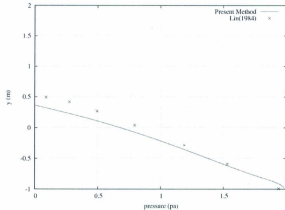


Figure 3-13 Pressure distribution on the wavemaker at $t=0.40s$

It can be seen that the results obtained by present method and Lin's method agree well in general. The small discrepancies could be caused by the different methods used for computing the time derivative of velocity potential, which is a significant component of pressure. Lin used finite difference method to get the time derivative of velocity potential while the time derivative of velocity potential was directly solved from the BEM in this work.

The force acting on the wavemaker were computed by integrating pressure along the surface of wavemaker, and are shown in Fig. 3-14. Despite the varying free surface elevations at each time instant, it can be seen that the force is insensitive in time in both Lin's results and present results. Due to the fact that the pressure distributions predicted by present method are slightly less than those by Lin's method, hence the resultant forces are also less than Lin's results.

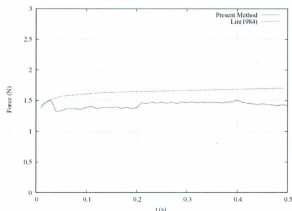


Figure 3-14 Horizontal force acting on the wavemaker

3.2 Symmetric water entry of 2-D Wedges

For the cases of symmetric 2-D wedges entering water, the computations were first carried out for wedges with deadrise angles of 30, 45 and 60 degrees. The free surface elevations and pressure distributions on wedge surface were computed and compared with results by the similarity method, BEM (Zhao, 1993) and the CIP method (Yang, 2007).

3.2.1 Grid generation in the chosen domain

A fluid domain with a length of 10m and a depth of 1m was chosen for the numerical simulation. No separation was considered in this problem. Due to the symmetric property of this problem about the y-axis, only half of the domain ($x>0$) was studied. The domain boundaries are divided by straight line segments, as shown in Fig. 3-15



Figure 3-15 Grids on the fluid domain boundaries

An enlarged view of the local region near the intersection point of the free surface and wedge is given in Fig. 3-16. It can be seen that the denser grids were used in the region near the intersection point. Note that the sizes of elements between two adjacent surfaces are comparable so that the computational stability can be achieved. On the wedge surface, the size of the elements was equal. On the bottom and the right-end wall surface, larger but equal-sized elements were distributed. On the free surface, the first 20 elements were of equal size for the smoothing scheme to be used, and the size of elements gradually increases as far from the wedge on the rest of the free surface.

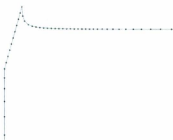


Figure 3-16 Grids near the intersection point

To facilitate the simulation of wedges entering water, computation was started initially with wedges slightly submerged into water. The apex of wedge was located at $y=$

-0.01m at $t=0^+$. Since there is a rapid change in the free surface profile at the initial water entry stage, especially for a wedge with a small deadrise angle, Wagner's approximation method (Sun, 2007) was employed to represent the initial free surface elevation when gravity is negligible. The constant velocity of wedge entering water was set to 2m/s.

3.2.2 Free surface elevations and pressure distributions

To investigate the convergence of pressure distribution for different sizes of grids on wedge surface, three different grid sizes are used in computation and results are compared for wedge with the deadrise angle of 30 degrees. The grid size on the free surface near the intersection area is set as 0.005m. The chosen grid sizes on wedge are 0.00866m, 0.00692m and 0.0052m. The results are given in Fig. 3-17.

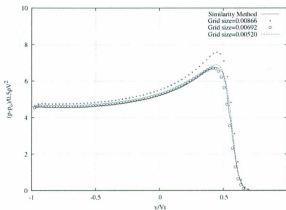


Figure 3-17 Pressure distributions for different grid sizes on wedge

It can be seen that the results agree with the similarity results best when the grid size on wedge surface equals 0.0052, which is closest to the size of grids on the free surface near the intersection point. This also proves that comparable size of grids on two adjacent surfaces is desirable in the computation as indicated in the wavemaker

case.

As mentioned above, equal-sized grids were employed in the region near the intersection point of free surface and wedge surface, and larger size of grids used on the rest of free surface. To investigate the influence of the length of the equal-sized grids on the free surface profile, the equal-sized grids were distributed in the range of 0.04m, 0.05m and 0.06m from the intersection point at the start of computation, respectively. The size of equal-sized grids was set as 0.002m for all tests. The results are shown in Fig. 3-18.

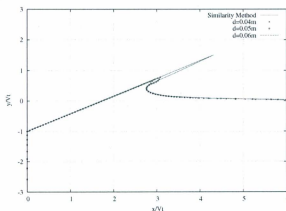


Figure 3-18 Free surface elevations for different lengths of equal-sized grids

It can be seen that the lengths of equal-sized grids are used in the computation do not have a great impact on the free surface profile. The reason for employing equal-sized grids is that the smoothing scheme can only be applied to evenly-spaced points. It should be noted that this area gets greater as the deadrise angles decrease.

The time histories of free surface elevations for the wedge with deadrise angle of 60 degrees from 0.006s to 0.03s at an increment of 0.006s are shown in Fig. 3-19 to Fig. 3-23. The results are nondimensionalized by dividing Vt , and V is the velocity of wedge entering water and t is the time instant. The results are compared with solutions

by the similarity method and experimental results (Greenhow and Lin, 1983), as shown in Fig. 3-24. It can be seen that the agreement between the present results and other solutions is in general good. In the beginning stage of the simulation, small discrepancies around the jet spray root area are shown in Fig. 3-19 and Fig. 3-20. However, the discrepancies disappear as the computation becomes steady as shown in Fig. 3-21, Fig. 3-22 and Fig. 3-23.

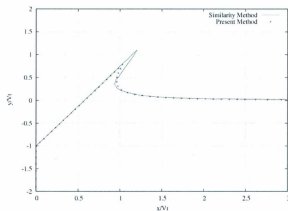


Figure 3-19 Free surface elevation of the wedge with deadrise angle of 60° at $t=0.006s$

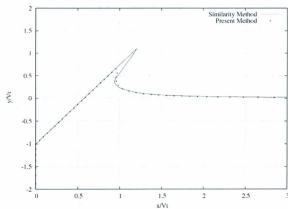


Figure 3-20 Free surface elevation of the wedge with deadrise angle of 60° at $t=0.012s$

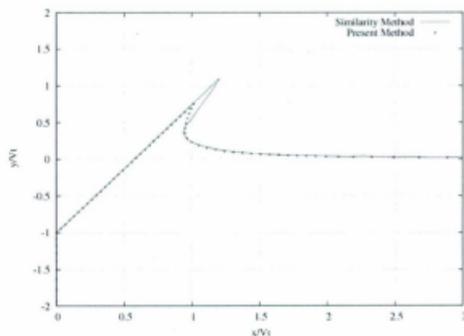


Figure 3-21 Free surface elevation of the wedge with deadrise angle of 60° at $t=0.018s$

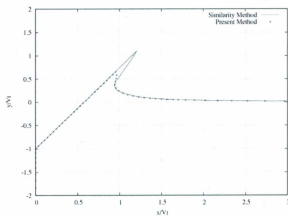


Figure 3-22 Free surface elevation of the wedge with deadrise angle of 60° at $t=0.024s$

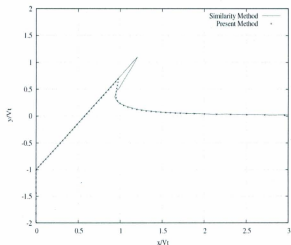


Figure 3-23 Free surface elevation of the wedge with deadrise angle of 60° at $t=0.03s$

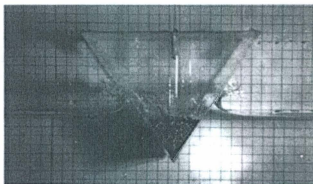


Figure 3-24 Snapshot of water entry of wedge with deadrise angle of 60° (Lin, 1983)

In the present method, only part of the thin jet flow was simulated in the computation and compared with the similarity solution.

Fig. 3-25 to Fig. 3-29 show the time histories of pressure distributions on the wedge surface with deadrise angle of 60 degrees from 0.006s to 0.03s at an increment of 0.006s. The results are nondimensionalized by dividing $0.5 \rho V^2$, where ρ is the water density and V is the velocity of wedge entering water. The results are compared with the solutions by the similarity method in the first four figures, and compared with other results by the CIP method (Yang, 2007) and BEM (Zhao, 1993) in Fig. 3-29. Good agreement with other solutions can be observed in those figures. The results by the present method are slightly smaller than the similarity solutions in Fig. 3-25 and Fig. 3-28 while the present results are slightly bigger than the similarity solutions in Fig. 3-27 and Fig. 3-29. However, in the duration of the simulation, it was shown that the results were steady without violent fluctuations. The results agree well with similarity solutions even in the very beginning of the simulation, which may suggest that the small discrepancies in free surface profile have limited impact on the pressure distribution. The slight variation of the pressure distribution over the process of simulation could be caused by rigidding of the free surface at each time instance.

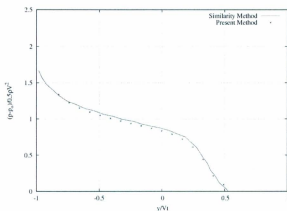


Figure 3-25 Pressure distribution on wedge with deadrise angel of 60° at t=0.006s

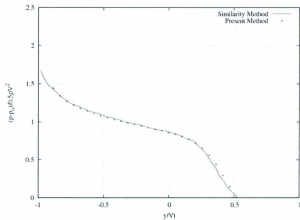


Figure 3-26 Pressure distribution on wedge with deadrise angle of 60° at $t=0.012s$

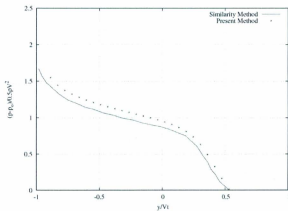


Figure 3-27 Pressure distribution on wedge with deadrise angle of 60° at $t=0.018s$

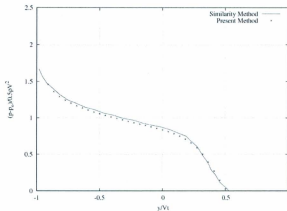


Figure 3-28 Pressure distribution on wedge with deadrise angle of 60° at $t=0.024s$

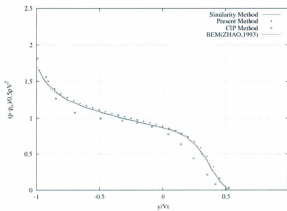


Figure 3-29 Pressure distribution on wedge with deadrise angle of 60° at $t=0.03s$

The same computational procedure was applied to a wedge with deadrise angle of 45 degrees from 0.006s to 0.03s at an increment of 0.006s. The time histories of free surface elevations are shown in Fig. 3-30 to Fig. 3-34. The results are compared with

solutions by the similarity method and experimental results (Greenhow and Lin, 1983), as shown in Fig. 3-35. In general, the present results are in good agreement with the similarity solutions. The discrepancies around the jet spray root area shown in Fig. 3-30 almost disappear as the computation becomes steady. Same as in the last case, the upper part of the thin jet is cut off, which does not affect the rest of the free surface profile.

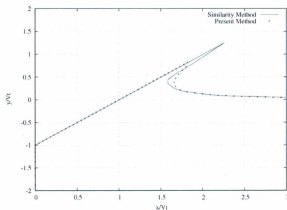


Figure 3-30 Free surface elevation of the wedge with deadrise angle of 45° at $t=0.006s$

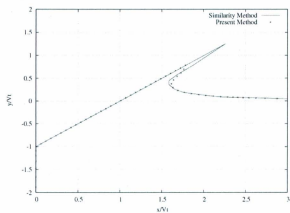


Figure 3-31 Free surface elevation of the wedge with deadrise angle of 45° at $t=0.012s$

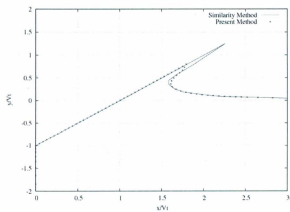


Figure 3-32 Free surface elevation of the wedge with deadrise angle of 45° at $t=0.018s$

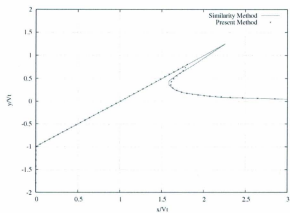


Figure 3-33 Free surface elevation of the wedge with deadrise angle of 45° at $t=0.024s$

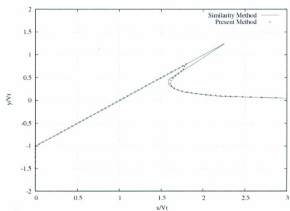


Figure 3-34 Free surface elevation of the wedge with deadrise angle of 45° at $t=0.03s$

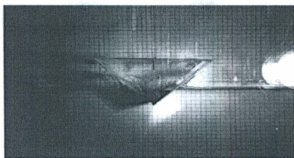


Figure 3-35 Snapshot of water entry of wedge with deadrise angle of 45° (Lin, 1983)

Fig. 3-36 to Fig. 3-40 show the time histories of pressure distributions on the wedge surface with deadrise angle of 45 degrees from 0.006s to 0.03s at an increment of 0.006s. The results are compared with the solutions by the similarity method.

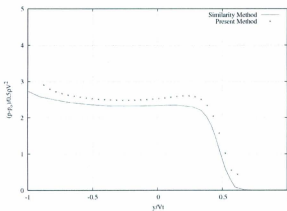


Figure 3-36 Pressure distribution on wedge with deadrise angle of 45° at $t=0.006$ s

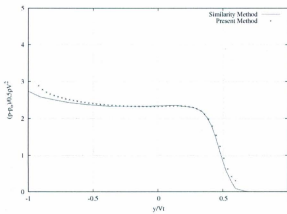


Figure 3-37 Pressure distribution on wedge with deadrise angle of 45° at t=0.012s

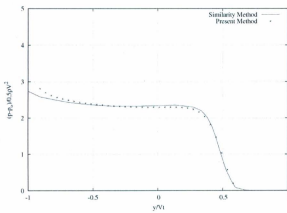


Figure 3-38 Pressure distribution on wedge with deadrise angle of 45° at t=0.018s

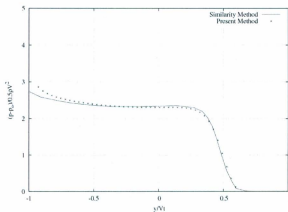


Figure 3-39 Pressure distribution on wedge with deadrise angle of 45° at $t=0.024s$

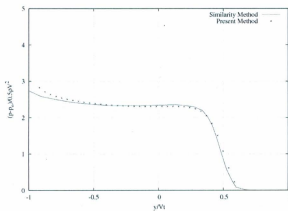


Figure 3-40 Pressure distribution on wedge with deadrise angle of 45° at $t=0.03s$

It can be seen that the results of pressure distributions by the present method are in good agreement with the similarity solution. The simulation was then carried out for a wedge with deadrise angle of 30° degrees. The time histories of free surface elevations at

$t=0.024s, 0.03s, 0.039s, 0.048, 0.057s$ are shown in Fig. 3-41 to Fig. 3-45. The results are compared with solutions by the similarity method. It can be seen that the agreement between the present results and similarity solutions is, in general, good. It should be noted that it took more time steps in this case to achieve the similarity results than the previous cases.

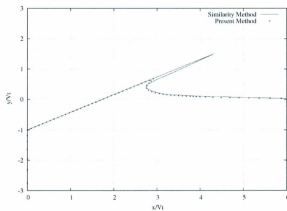


Figure 3-41 Free surface elevation of the wedge with deadrise angle of 30° at $t=0.024s$

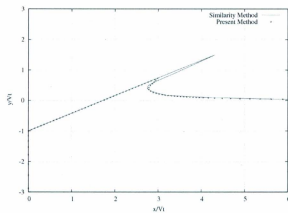


Figure 3-42 Free surface elevation of the wedge with deadrise angle of 30° at $t=0.03s$

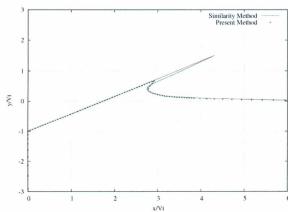


Figure 3-43 Free surface elevation of the wedge with deadrise angle of 30° at $t=0.039s$

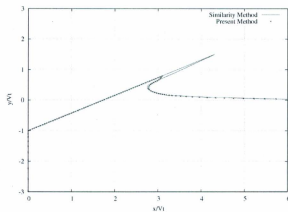


Figure 3-44 Free surface elevation of the wedge with deadrise angle of 30° at $t=0.048s$

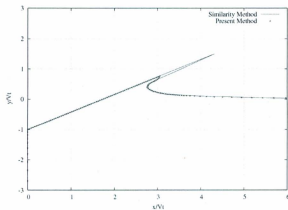


Figure 3-45 Free surface elevation of the wedge with deadrise angle of 30° at $t=0.057s$

Fig. 3-46 to Fig. 3-50 show the time histories of pressure distributions on the wedge surface with deadrise angle of 30 degrees at $t=0.024s, 0.03s, 0.039s, 0.048, 0.057s$. The results are compared with the solutions by the similarity method in the first four

figures, and compared with other results by the CIP method (Yang, 2007) and BEM (Zhao, 1993) in Fig. 3-50. In general, the present results show good agreement with the other solutions.

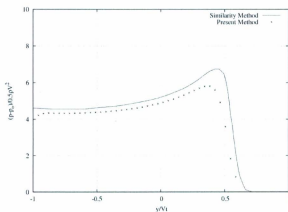


Figure 3-46 Pressure distribution on the wedge with deadrise angle of 30° at $t=0.024s$

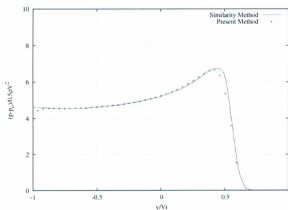


Figure 3-47 Pressure distribution on the wedge with deadrise angle of 30° at $t=0.03s$

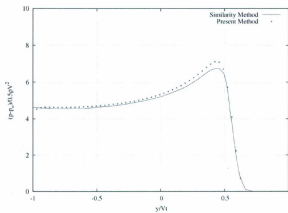


Figure 3-48 Pressure distribution on the wedge with deadrise angle of 30° at $t=0.039s$

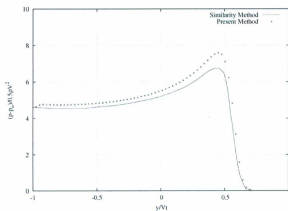


Figure 3-49 Pressure distribution on the wedge with deadrise angle of 30° at $t=0.048s$

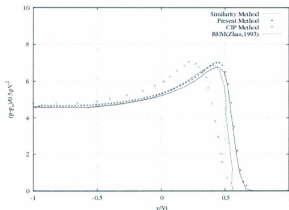


Figure 3-50 Pressure distribution on the wedge with deadrise angle of 30° at $t=0.057s$

3.3 Symmetric water entry of 2-D wedges with various deadrise angles

Free surface elevations and pressure distributions on wedges with various deadrise angles were also computed by the present method. The deadrise angles varied from 10 to 81 degrees. Due to the limited access to results generated by other methods, comparisons of the present results were only made with those from the similarity method, BEM (zhao, 1993) and the CIP method (Yang, 2007) for deadrise angle of 40 degrees. The free surface results are shown in Fig. 3-63 while Fig. 3-64 presents the results of pressure distributions. In addition, comparisons were also made between the present results and similarity solutions for deadrise angles of 81, 25, 20, 15, and 10 degrees, as shown in Fig. 3-51, Fig. 3-52 and Fig. 3-67 to Fig. 3-74.

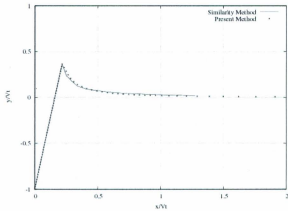


Figure 3-51 Free surface elevation of the wedge with deadrise angle of 81° at $t=0.045s$

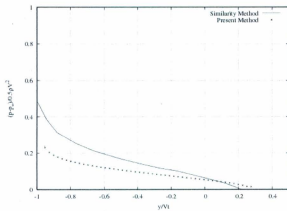


Figure 3-52 Pressure distribution on the wedge with deadrise angle of 81° at $t=0.045s$

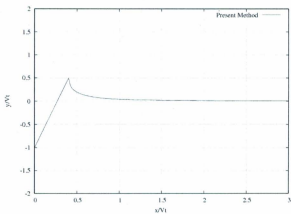


Figure 3-53 Free surface elevation of the wedge with deadrise angle of 75° at $t=0.045s$

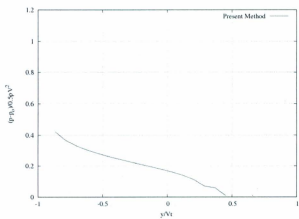


Figure 3-54 Pressure distribution on the wedge with deadrise angle of 75° at $t=0.045s$

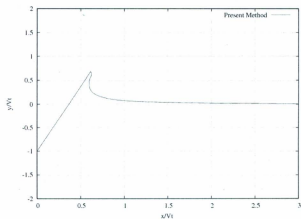


Figure 3-55 Free surface elevation of the wedge with deadrise angle of 70° at $t=0.057s$

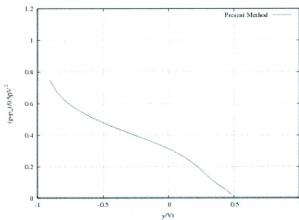


Figure 3-56 Pressure distribution on the wedge with deadrise angle of 70° at $t=0.057s$

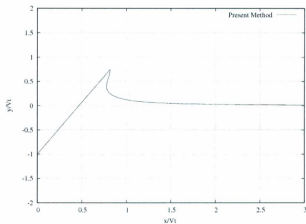


Figure 3-57 Free surface elevation of the wedge with deadrise angle of 65° at $t=0.057s$

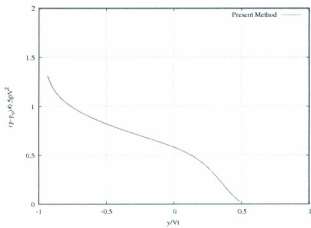


Figure 3-58 Pressure distribution on the wedge with deadrise angle of 65° at $t=0.057s$

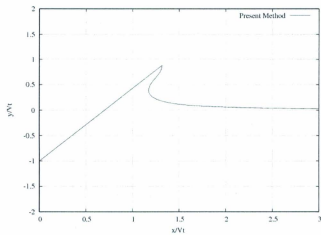


Figure 3-59 Free surface elevation of the wedge with deadrise angle of 55° at $t=0.024s$

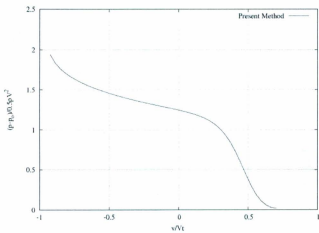


Figure 3-60 Pressure distribution on the wedge with deadrise angle of 55° at $t=0.024s$

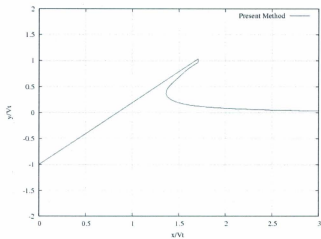


Figure 3-61 Free surface elevation of the wedge with deadrise angle of 50° at $t=0.024s$

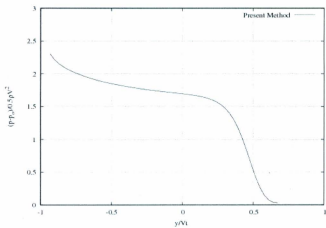


Figure 3-62 Pressure distribution on the wedge with deadrise angle of 50° at $t=0.024s$

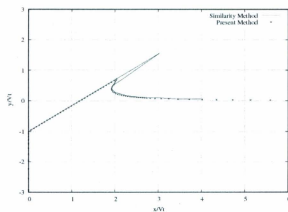


Figure 3-63 Free surface elevation of the wedge with deadrise angle of 40° at $t=0.036s$

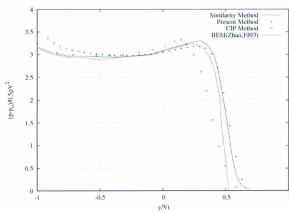


Figure 3-64 Pressure distribution on the wedge with deadrise angle of 40° at $t=0.036s$

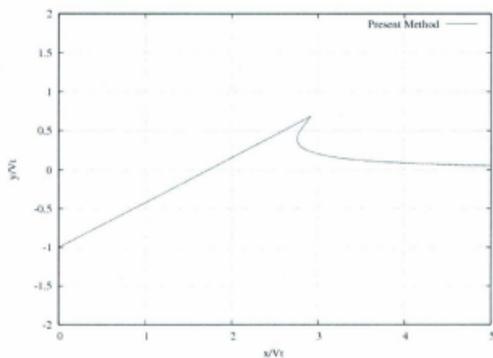


Figure 3-65 Free surface elevation of the wedge with deadrise angle of 35° at $t=0.036s$

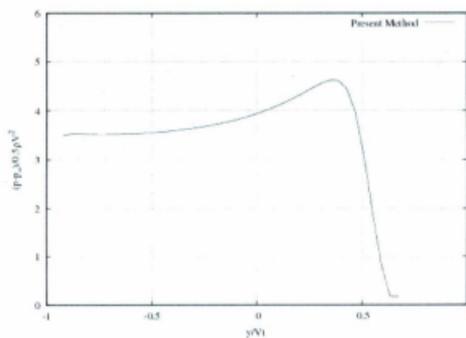


Figure 3-66 Pressure distribution on the wedge with deadrise angle of 35° at $t=0.036s$

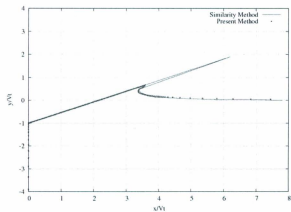


Figure 3-67 Free surface elevation of the wedge with deadrise angle of 25° at $t=0.036s$

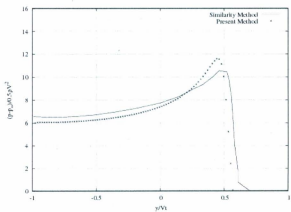


Figure 3-68 Pressure distribution on the wedge with deadrise angle of 25° at $t=0.036s$

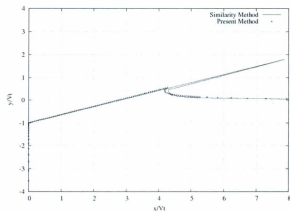


Figure 3-69 Free surface elevation of the wedge with deadrise angle of 20° at $t=0.036s$

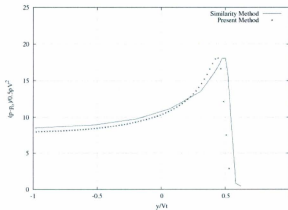


Figure 3-70 Pressure distribution on the wedge with deadrise angle of 20° at $t=0.036s$

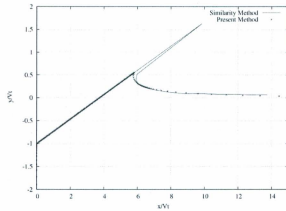


Figure 3-71 Free surface elevation of the wedge with deadrise angle of 15° at $t=0.0495s$

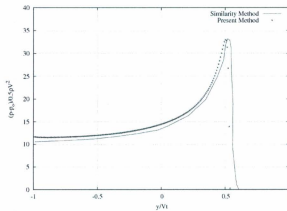


Figure 3-72 Pressure distribution on the wedge with deadrise angle of 15° at $t=0.0495s$

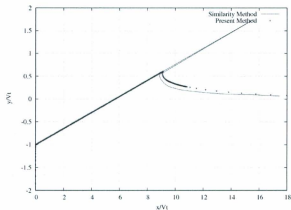


Figure 3-73 Free surface elevation of the wedge with deadrise angle of 10° at $t=0.0558s$

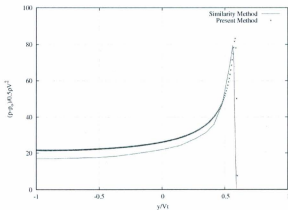


Figure 3-74 Pressure distribution on the wedge with deadrise angle of 10° at $t=0.0558s$

From the above figures, it can be observed that the agreement between the present results (free surface elevations and pressure distributions) and other solutions is generally good. The largest differences occur in the prediction of the free surface

profile close to the jet flow. This could be associated with the jet flow cut-off technique implemented in the computation. As the deadrise angle increases, the jet flow becomes less apparent and the maximum pressure sharply decreases. The position of the maximum pressure occurred close to the jet root region for deadrise angles less than 45 degrees. When the deadrise angle is equal to or larger than 45 degrees, the maximum pressure is at the apex of the wedge. In Fig. 3-50, the pressure for deadrise angle of 81 degrees, predicted by the present method, is smaller than that by the similarity method. This could be explained by the singularity at the apex of wedges with large deadrise angles, as pointed out by Yim (1987). The singularity was avoided using constant elements. However, it still has influence on the distribution of velocity potential on the wedge surface, which leads to inaccurate pressure prediction. In addition, it can be deduced that the effect of the singularity at the apex of wedges becomes greater with the increase of deadrise angles.

Chapter4 Conclusions

The nonlinear problem of symmetric water entry of 2-D wedges governed by the Laplace equation was solved by a numerical method that was developed based on the BEM. In the computation, the Laplace equation was numerically solved at each time instant using the BEM. The boundary conditions for the next time step were updated by a time marching procedure. The free surface was captured by the MEL method and smoothed out by the five-point smoothing scheme to eliminate any sawtooth phenomenon. The free surface was then regrided by parametric Cubic Splines to avoid overly dense or scarce segments near the intersection region. A cut-off treatment was performed for the thin jet flow near the intersection points to maintain computational stability. For the pressure calculation, the time derivative of velocity potential with boundary conditions was solved using the BEM and the pressure can then be obtained using Bernoulli's equation.

Validation studies have been carried out for an impulsive wavemaker and symmetric wedges with various deadrise angles. For the case of impulsive wavemaker, pressure distributions, free surface elevations and hydrodynamic forces were computed and compared with the analytical solutions and results by Lin (1983)'s method. For the 2-D wedges problem, pressure distributions and free surface elevations were computed and compared with the similarity method, the CIP method (Yang, 2007) and results by BEM (Zhao, 1993). The results by the present method are generally in good agreement with others. It has been demonstrated that the numerical method developed in this work is able to solve the nonlinear body-water interaction problems with highly distorted free surface and provide good predictions of free surface elevations and pressure distributions on wavemaker or wedges with a range of deadrise angles.

For future work, studies can be extended to the problem of symmetric wedges entering water with separation points, asymmetric wedges water entry problem, and three-dimensional water entry problem of bodies of arbitrary geometry.

References

Armand, J.L and Cointe, R, 1986, Hydrodynamic impact analysis of a cylinder, Proceedings of Fifth International Offshore Mechanics and Arctic Engineering, Vol.1, pp. 609-634.

Battistin, D and Iafrat, A, 2003, Hydrodynamic loads during water entry of two-dimensional and axisymmetric bodies, Journal of Fluids and Structures, Vol. 17, pp.643 - 664.

Burden,R and Faires,J, 2005, Numerical Analysis, Thomson Brooks.

Chuang, J.M., Zhu, W. and Qiu, W., 2006, Numerical solutions of 2D water entry problem, ISOPE, San Francisco.

Cointe, R. and Howison, 1991, Free surface flows close to a surface-piercing body, Mathematical Approaches in Hydrodynamics, pp. 319-334.

Dobrovol'skaya, Z.N., 1969, On some problems of similarity flow of fluid with a free surface, Journal of Fluid Mechanics, Vol. 36, pp. 805-829.

Faltinsen, O., 1990, Sea Loads on Ships and Offshore Structures, Cambridge University Press.

Faltinsen, O., Maurizio Landrini and Mrileana Greco, 2004, Slamming in marine applications, Journal of Engineering Mathematics, Vol.48 pp. 187-217.

Greenhow, M., 1987, wedge entry into initially calm water, Applied Ocean Research,

Vol.9, pp. 214-223.

Greenhow, M. and Lin, W.M., 1983, Nonlinear free surface effects: experiments and theory, Report No.83-19, Department of Ocean Engineering, MIT, Cambridge, MA.

Howison, S.D., Ockendon, J.R. and Wilson, S.K., 1991, Incompressible water-entry problems at small deadrise angles, *Journal of Fluid Mechanics*, Vol. 222, pp. 215-230.

Kihara H, 2004, Numerical modeling of flow in water entry of a wedge, Proceedings of 19th International Workshop on Water Waves and Floating Bodies, Italy, pp. 200-213.

Kihara, H, 2008, A numerical study for bow flare slamming analysis using boundary element method, Proceedings of 6th Osaka Colloquium on Seakeeping and Stability of Ships, pp.179-186.

Kim, Y.W., Kim, Y., Liu, Y.M., and Yue, D., 2007, On the water-entry impact problem of asymmetric bodies, 9th International Conference on Numerical Ship Hydrodynamics, Michigan.

Kleefsman, K.M.T., Fekken, G., Veldman, A.E.P., Iwanowski, B. and Buchner, B., 2005, A volume-of-fluid based simulation method for wave impact problems, *Journal of Computational Physics*, Vol. 206, pp. 363-393.

Kythe, P, 1995, An introduction to boundary element method, CRC Press.

Lin, M.C and Ho, T.Y, 1994, Water-entry for a wedge in arbitrary water depth, *Engineering Analysis with Boundary Elements*, Vol. 14, pp. 179-185.

Lin, W.M., Newman, J.N. and Yue, D.K., 1984, Nonlinear forced motions of floating

bodies, Proceedings of the 15th Symposium on Naval Hydrodynamics, Hamburg, pp. 33-47.

Lin, W.M., 1984, Nonlinear motion of the free surface near a moving body, Ph.D. thesis, MIT, Cambridge, LA.

Longuet-Higgins, M.S., and Cokelet, E.D, 1976, The deformation of steep surface waves on water. A numerical method of computation, Proceedings of the Royal Society of London. Series A 350, Mathematical and Physical Sciences, pp. 1-26.

Qian, K and Wang, Y.Y, 2005, Time-domain prediction of nonlinear motions and loads of body in large waves using a high order panel method, Proceedings of 15th International Offshore and Polar Engineering Conference, Seoul, Korea, pp. 132-137.

Roache, Patrick, 1972, Computational Fluid Dynamics, Hermosa Publishers.

Schwartz, L.M., and Fenton, L.D., 1982, Strongly nonlinear waves, Journal of Fluid Mechanics, Vol. 14, pp.39-60.

Sun, Hui, 2007, A boundary element method applied to strongly nonlinear wave-body interaction problems, Ph.D. thesis, Norwegian University of Science and Technology, Trondheim, Norway.

Tanizawa, K, 1995, A nonlinear simulation method of 3-D body motion in waves, Journal of the Society of Naval Architecture, Japan, Vol.178, pp. 179-191.

Tveitnes T., Fairlie-Clarke A.C., Varyani K., 2008, An experimental investigation into the constant velocity water entry of wedge-shape sections, Journal of Ocean Engineering, Vol. 35, pp. 1463- 1478.

Vinje, T. and Brevig, P., 1981, Numerical simulation of breaking waves, *Adv Water Resources*, Vol. 4, pp. 77-82.

Von Karman, 1929, The impact of seaplane floats during landing, *Nat. Adv. Com. for Aeronautics. Note 321*, pp. 309-313.

Wu, G.X., Xu, G.D., and Duan, W.Y., 2010, A summary of water entry problem of a wedge based on the fully nonlinear velocity potential theory, 9th International Conference on Hydrodynamics, Shanghai, China.

Yang, Qingyong, 2007, Numerical solution of 2-D slamming problem with a CIP method, Master thesis, Memorial University of Newfoundland, Newfoundland, Canada.

Yim, B., 1985, Numerical simulation for two-dimensional wedge slamming with a nonlinear free surface condition, *Proceedings of 4th International Conference on Numerical Ship Hydrodynamics*, pp. 107-116.

Zhao, R and Faltinsen, O.M., 1993, Water entry of two dimensional bodies, *Journal of Fluid Mechanics*, Vol. 246, pp. 593-612.

Zhao, R and Faltinsen, O.M., 1996, Water entry of arbitrary two dimensional sections with and without flow separation, *Proceedings of 21st Symposium on Naval Hydrodynamics*, Trondheim, Norway.



